# Time evolution of dehydration-induced stick-slip behaviors of simulated bassanite gouges

Rei Shiraishi[1], Mikihiro Kawabata[1], Jun Muto[1], Hiroyuki Nagahama[1], Yuto Sasaki[2], and Masaaki Iwasaki[3]

[1]Tohoku University
[2]Kaijo Junior and Senior High School
[3]Dia Nippon Engineering Consultants Co., Ltd.

April 16, 2024

## Abstract

Pore fluid pressure generated by dehydration of hydrous minerals can trigger deep and intermediate-depth earthquakes. To investigate its effect on frictional behaviors, we conducted friction experiments on simulated bassanite gouges and observed the stress drops and recurrence intervals of stick-slip events decreased over time under 200 MPa and 110 °C. Microstructural observations indicates that gouges deformed under room temperature shows the development of numerous shear bands including Riedel shears. On the other hand, a sample deformed under 200 MPa and 110 °C had few Riedel shear planes, indicative of the elevated pore fluid pressure suppressing the development of shear planes. We derived time function of dehydration-driven pore fluid pressure evolution using Avrami kinetics. Because of the mathematical similarity of Avrami equation and the fractal geometry, our result shows that the kinetics-driven pore fluid pressure evolution controlled the stick-slip behaviors of the basanite gouges under dehydration.

## Hosted file

`Kawabata etal to GRL.docx` available at [https://authorea.com/users/741793/articles/714017-time-evolution-of-dehydration-induced-stick-slip-behaviors-of-simulated-bassanite-gouges](https://authorea.com/users/741793/articles/714017-time-evolution-of-dehydration-induced-stick-slip-behaviors-of-simulated-bassanite-gouges)

## Hosted file

`AGU_SuppInfo_Kawabata.docx` available at [https://authorea.com/users/741793/articles/714017-time-evolution-of-dehydration-induced-stick-slip-behaviors-of-simulated-bassanite-gouges](https://authorea.com/users/741793/articles/714017-time-evolution-of-dehydration-induced-stick-slip-behaviors-of-simulated-bassanite-gouges)

**AGU**

**PUBLICATIONS**

# Time evolution of dehydration-induced stick-slip behaviors of simulated bassanite gouges

**M. Kawabata[1], R. Shiraishi[1], J. Muto[1], H. Nagahama[1], Y. Sasaki[2], and M. Iwasaki[3]**

[1]Department of Earth Sciences, Graduate School of Science, Tohoku University, 6-3 Aramaki-Aza-Aoba, Aoba-ku, Sendai, Miyagi, 980-8578, Japan

[2]Kaijo Junior and Senior High School, 3-6-1 Okubo, Shinjuku-ku, Tokyo, 169-0072, Japan

[3]Dia Nippon Engineering Consultants Co., Ltd., 2-272-3 Yoshinocho, Saitamashi Kitaku, Saitama, 331-0811, Japan

Corresponding author: Rei Shiraishi (rei.shiraishi.b5@tohoku.ac.jp )

**Key Points:**

- During friction experiments on simulated bassanite gouges, pore pressure occurred due to the dehydration of bassanite.

- The Avrami kinetics of dehydration bassanite represented the information on pore structures.

- The amount of slip of deformation was controlled by dehydration kinetics of hydrous minerals.

27    **Abstract**

28    Pore fluid pressure generated by dehydration of hydrous minerals can trigger deep and

29    intermediate-depth earthquakes. To investigate its effect on frictional behaviors, we conducted

30    friction experiments on simulated bassanite gouges and observed the stress drops and recurrence

31    intervals of stick-slip events decreased over time under 200 MPa and 110 °C. Microstructural

32    observations indicates that gouges deformed under room temperature shows the development of

33    numerous shear bands including Riedel shears. On the other hand, a sample deformed under 200

34    MPa and 110 °C had few Riedel shear planes, indicative of the elevated pore fluid pressure

35    suppressing the development of shear planes. We derived time function of dehydration-driven

36    pore fluid pressure evolution using Avrami kinetics. Because of the mathematical similarity of

37    Avrami equation and the fractal geometry, our result shows that the kinetics-driven pore fluid

38    pressure evolution controlled the stick-slip behaviors of the basanite gouges under dehydration.

39

40    **Plain Language Summary**

41    The dehydration of hydrous minerals is one of the mechanisms of deep and intermediate-depth

42    earthquakes in the subduction zone. We conducted friction experiments on simulated calcium

43    sulfate hemihydrate gouges. Pore fluid pressure was observed as a result of dehydration of

44    hydrous minerals. We showed that the dehydration kinetics of hydrous minerals controlled the

45    stick-slip behavior.  We expect to estimate the seismogenesis of deep and intermediate-depth

46    earthquakes in the subduction zone based on dehydration kinetics.

47

48    **1 Introduction**

49        Reducing effective pressure, and resulting in dehydration embrittlement has been

50    proposed as one of the mechanisms of deep and intermediate-depth earthquakes in the

51    subduction zone (e.g., Raleigh & Paterson, 1965; Kirby, 1995; Brantut et al., 2012; Shiraishi et

52    al., 2022). This mechanism indicates that subducting hydrous minerals dehydrated at elevated

53    temperature and pressure generate pore fluid pressure, and reduce failure strengths (e.g., Raleigh

54    & Paterson, 1965; Yamasaki & Seno, 2003). However, whether dehydration of hydrous minerals

55    causes earthquakes is still under debate (Chernak & Hirth, 2011; Procter & Hirth, 2015).

56        Many deformation experiments for gypsum ($CaSO_4 \cdot 2H_2O$) have been conducted,

57    because it can dehydrate under relatively low temperature and low pressure and can easily

58    reproduce the dehydration process of hydrous minerals in the laboratory (e.g., Milsch & Scholz,

59    2005; Olgaard & Wong, 1995). Leclère et al. (2016) performed triaxial deformation experiments

60    using gypsum, and directly measured the variation of pore fluid pressure, which demonstrated

61    the decrease in strength due to dehydration-derived pore fluid pressure.

62        To study the dehydration kinetics of hydrous minerals, Perrillat et al. (2005) conducted

63    *in-situ* heating experiments using antigorite, a major mineral within subduction zones. The *in-*

64    *situ* analysis suggested that dehydration of antigorite obey the kinetic equation, Avrami theory.

65    Additionally, Chollet et al. (2009) also studied the dehydration kinetics of talc using dehydration

66    experiments conducted under high pressure and high temperature and showed that estimated

67    dehydration rate based on the kinetics data was greater than viscous relaxation rate of

68    surrounding materials. Since dehydration of hydrous minerals proceeds at a rate greater than the

69  viscous relaxation rate, the released water generates pore fluid pressure, which can reduce
70  mechanical strength and trigger intraplate earthquakes.

71      By combining two important elements, pore fluid pressure and dehydration kinetics, that
72  have been studied based on dehydration reactions of hydrous minerals, it is expected that time
73  variation of dehydration-derived pore fluid pressure can be quantitatively described. In this study,
74  we represent time evolution of pore fluid pressure, based on shear deformation experiments of
75  simulated bassanite (dehydrated gypsum, $CaSO_4 \cdot 0.5H_2O$) gouges associated with dehydration
76  instability. Under the assumption that pore fluid pressure was linearly proportional to
77  dehydration ratio, the behavior of pore fluid pressure calculated from the experimental results fits
78  well with Avrami kinetics.

79

## 80  2 Materials and Methods

81      We conducted triaxial shear deformation experiments using the high pressure gas
82  confining apparatus (PRETECH Co., LTD., Japan) installed at Tohoku University (Onuma et al.,
83  2011; Hirata et al., 2014; Jayawickrama et al., 2021). Bassanite ($CaSO_4 \cdot 0.5H_2O$) powders were
84  used as the starting materials. To begin with, we dried gypsum($CaSO_4$) under 60 °C for more
85  than a month in order to eliminate humidity. X-ray diffraction (XRD) revealed that the sample
86  after drying turned into bassanite. As gypsum is no longer stable over 40 °C in the atmosphere,
87  the phase transition from gypsum to bassanite could have occurred. The samples were cylindrical
88  cores (radius, 10 mm; height, 40 mm) with bassanite gouges (thickness of gouge, 0.5 mm;
89  particle size, 63 ~ 125 μm) sandwiched between gabbroic forcing blocks at an axial angle of 35
90  degrees. We covered the samples with a heat shrinkable tube indicating that the experiments
91  were conducted under undrained conditions. Before deformation experiments, all samples except
92  the one under 10MPa and room temperature (RT) were precompacted at room temperature for 30
93  minutes. In the precompaction, confining pressure was increased to 200 MPa without loading,
94  and then differential stress of 200 MPa was applied. In our experiments, we installed a load cell
95  on the lower piston of the assembly and a high-precision laser displacement transducer on the
96  upper piston to measure the load and displacement, respectively. The experimental conditions
97  were eight combinations of confining pressures and temperatures: 10 MPa and RT, 50 MPa and
98  RT, 100 MPa and RT, 150 MPa and RT, 200 MPa and RT, 200 MPa and 70 °C, 200 MPa and
99  110 °C, and 200 MPa and 110-180 °C (see Table S1 for strain rate). We set the 200 MPa and
100  maximum 180 °C condition to ensure that gypsum series can completely dehydrate. After the
101  experiments, we made thin sections using water-insoluble grinding oil to observe microstructures
102  using scanning electron microscope (SEM, JEOL 7001F).

103

## 104  3 Results

105      Figure 1 and S1 show stress-strain curves obtained from triaxial shear deformation
106  experiments on bassanite gouge samples under confining pressures up to 200 MPa and
107  temperatures ranging from room temperature to 180 °C. The experiments conducted under RT
108  with various confining pressures show the increase in peak strengths with confining pressures.
109  Moreover, periodic stick-slips occurred except for 10 MPa and RT condition (hereafter,
110  10MPa_RT), and the recurrence intervals of those slip events depended on confining pressures

111  (Figure 2). Additionally, the experiment conducted under high temperature but within a stability
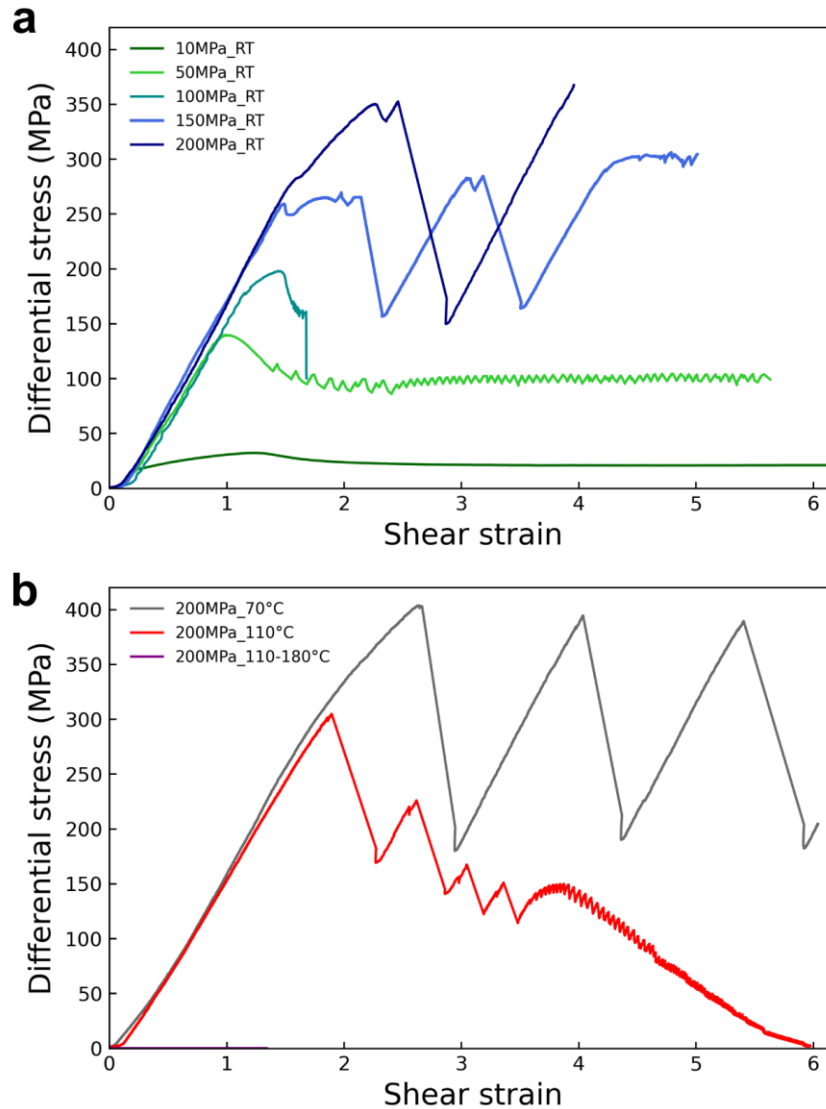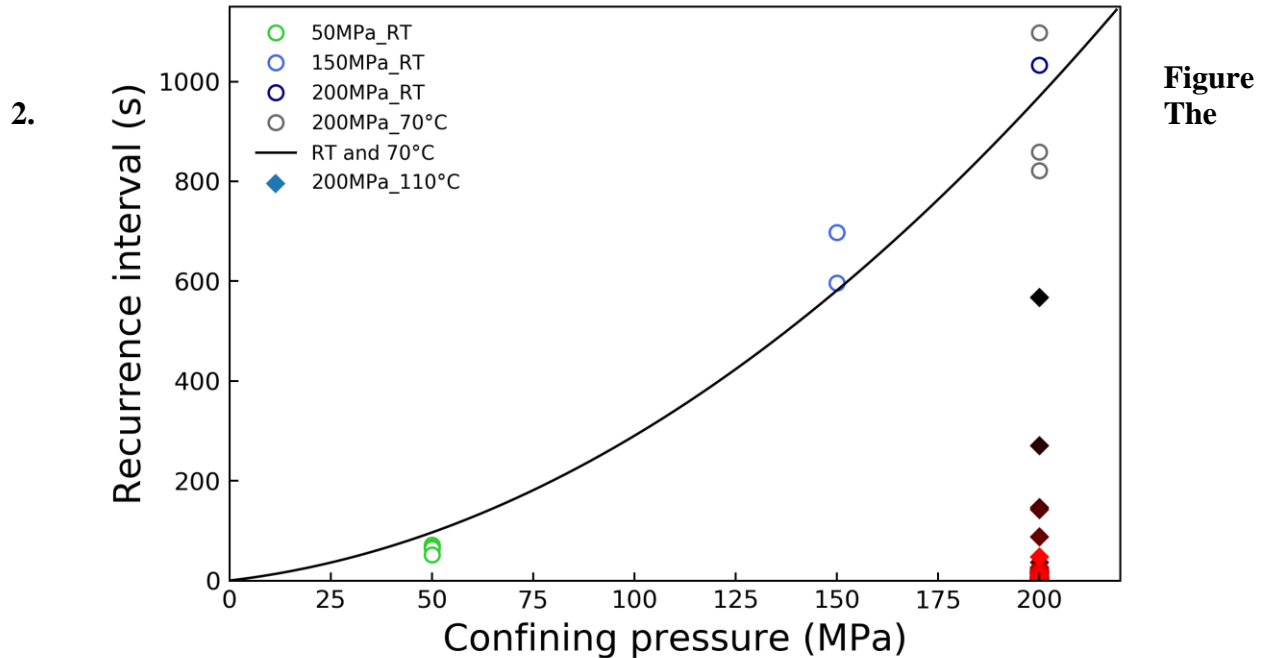112  field of gypsum (200MPa_70°C) showed the similar behavior to the one conducted under RT.

113

114

115



139  **Figure 1. Stress-strain curve during triaxial shear deformation experiments under eight**
140  **conditions.** Temperature conditions are (**a**) room temperature (denoted as RT), and (**b**) over 70
141  °C. The characters of legends are confining pressure (MPa) and temperature (°C). The results
142  under 70 °C or below showed almost constant differential stress, while the differential stress
143  under 200MPa_110°C (red plot) remarkably decreased with strain. The differential stress under
144  200MPa_110-180°C was relatively almost 0 MPa.

145

146

147

148

149

150

152 **2.**



**Figure The**

relationship between confining pressure (MPa) and recurrence interval (s).

153 **relationship between confining pressure (MPa) and recurrence interval (s).** Since no large
154 sharp stress drop event was observed under 10MPa_RT and under 200MPa_110-180°C and we
155 could not uniquely recognize recurrence interval under 100MPa_RT, we plotted the data under
156 other five conditions. The black curve is a quadratic fitting for RT and 70 °C conditions.
157 Regarding the data of 200MPa_110°C (diamond plot), we used gradient color scheme with black
158 for the first stress drop event data (corresponding to shear strain of about 1.9 in Fig. 1**b**) and red
159 for the last stress drop event data (corresponding to shear strain of about 5.9 in Fig. 1**b**). By
160 substituting each recurrence interval under 200MPa_110°C into the derived quadratic function,
161 we can estimate the effective pressure at each stress drop event.

162

163

164          The peak strengths, including the amount of stress drop and recurrence interval of slip
165 events, decreased over time in a sample deformed under 200MPa_110°C. Moreover, there was a
166 high positive correlation between recurrence intervals and the slip amounts of the preceding
167 events (Figure S2). This suggests that the stick-slip behavior under 200MPa_110°C follows
168 time-predictable recurrence model (Shimazaki & Nakata, 1980). Figure 2 shows the relationship
169 between confining pressures $P_c$ (MPa) and recurrence intervals $\Delta t$ (s) for five experiments. We
170 excluded the data under 10MPa_RT and 200MPa_110-180°C because we could not recognize
171 any slip events with clear stress drops in those experiments, and we also excluded the data under
172 100MPa_RT because we could not uniquely recognize recurrence interval. As the experiments

173 conducted under 70 °C or RT indicated a positive correlation between confining pressures and
174 recurrence intervals, we derived a regression curve from the data. Considering the negative
175 recurrence intervals extrapolated by a linear regression, we adopted a quadratic regression curve
176 and obtained the following equation:

$$\Delta t = aP_c^2 + bP_c, \#(1)$$

177 where $a$ is 0.0195 s· MPa$^{-2}$, and $b$ is 0.952 s·MPa$^{-1}$ (R$^2$ = 0.957). We set the constant to 0
178 as the minimum of recurrence interval should be 0, consistent with the experiment conducted
179 under 10 MPa.

180 X-ray diffraction (XRD) analysis for the starting material and recovered gouges revealed
181 that the sample deformed under 200 MPa and 110-180 °C was transformed to anhydrite
182 (dehydrated bassanite, CaSO$_4$); however, other samples including the one under 200MPa_110°C
183 remained bassanite (Figure 3).

184 Representative microstructures in the recovered samples are shown in Figure 4 and S3.
185 We recognized Riedel (R1) shear planes in samples deformed under 200MPa_RT and
186 200MPa_70°C (Figure 4a and 4b). In the sample deformed under 200MPa_110°C, despite
187 multiple large stress drops, most of the identified cracks were perpendicular to the shear zone
188 boundary (Figure 4c) and only a few Riedel shear planes existed (Figure 4d). In the sample
189 deformed under 200MPa_110-180°C, P shear planes (oblique in the opposite direction to the
190 Riedel shear planes) were confirmed in addition to Riedel shear planes, and some areas of the
191 slip boundary were found to be missing.

192

193

194

195

196

197

198

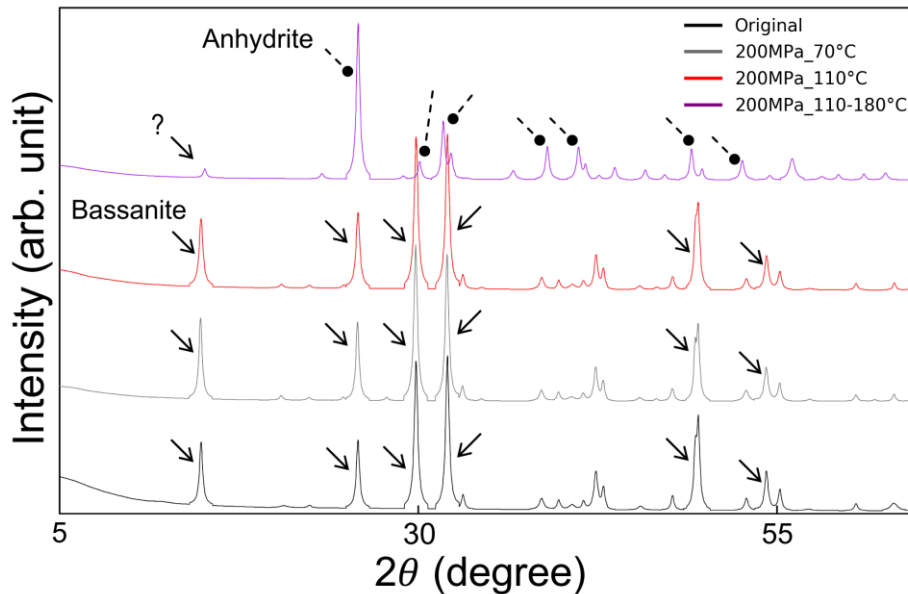199

200

201

202

203

204

205



206 **Figure 3. The results of X-ray diffraction.** The arrows and dots indicate the locations of
207 bassanite and anhydrite, respectively. The peak at about 15° of the sample deformed under
208 200MPa_110-180°C could not be identified. The sample under 200MPa_110-180°C was
209 revealed as anhydrite. However, the others, including the sample under 200MPa_110°C which

210 showed the reduction in the amount of stress drop and recurrence interval with time, turned out
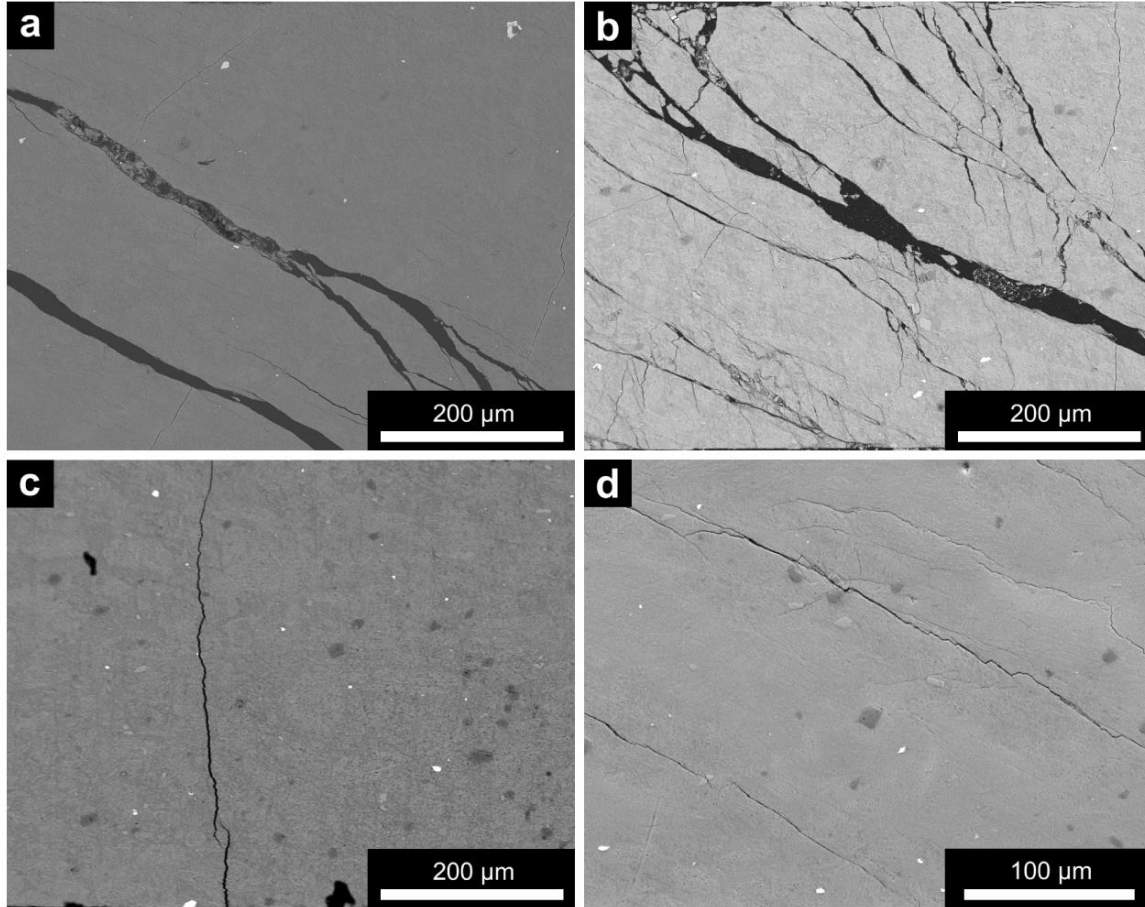211 to be bassanite.

212



213
214 **Figure 4. Microstructures of deformed samples under confining pressures of 200 MPa**
215 **obtained by scanning electron microscopy.** The senses of shears are dextral. The temperature
216 conditions were RT (**a**), 70 °C (**b**), and 110 °C (**c** and **d**). Riedel shear planes have developed on
217 the microstructures under RT (**a**) or 70 °C (**b**). Commonly observed microstructures under
218 110 °C were cracks perpendicular to the shear plane (**c**) although we were able to confirm a few
219 Riedel shear planes under 110 °C (**d**).

220

221

222

223

224

225

226

227

228

**4 Discussion**

4.1 Dehydration triggering the reduction in frictional strength

In the experiment conducted under 200MPa_110°C, differential stresses and recurrence intervals gradually decreased with strain (Figure 1b) despite that the experiment was conducted under the constant confining pressure. The experiments conducted under RT showed that the recurrence intervals were dependent on confining pressures (Figure 2), which implies temporal change in effective pressure in the experiment conducted under 200MPa_110°C. XRD analysis clarified that only the sample deformed under 200MPa_110-180°C was transformed into anhydrite. In other words, the sample deformed under 200MPa_110°C did not dehydrate and remained the same as the starting material after the experiment. However, among calcium sulfate hydrates, anhydrite is the most stable above 75 °C under 200 MPa (Mirwald, 2008). Additionally, it has been clarified that anhydrite can absorb water vapor in the air to form bassanite (Tang et al., 2019). These imply that the sample deformed under 200MPa_110°C was dehydrated under the experimental condition and rehydrated again into the bassanite. Therefore, in the discussion, we first discuss the possibility of dehydration of bassanite gouges under 200MPa_110°C.

Previous experiments of simulated gouges have reported the formation of continuous Riedel (R1) shear planes (Leclère et al., 2016; Gu & Wong, 1994; Onuma et al., 2011; Hirauchi & Muto, 2015). From the friction experiment conducted under semi-undrained conditions using gypsum gouge, Leclère et al. (2016) demonstrated few Riedel shear planes under the low shear stress condition due to elevated pore fluid pressure by dehydration. Furthermore, they reported the continuous development of Riedel shear planes under fully drained condition where the elevated pore pressure escaped from the gouge and the shear stress reached its maximum. These results suggest that the elevated pore fluid pressure within the gouges inhibits the development of the localized shear planes in the gypsum gouge. Thus, scarce development of the Riedel shear planes in the sample deformed under 200MPa_110°C supports the generation of pore fluid pressure during the deformation experiment.

Since microstructural observations suggested that pore fluid pressure may have been elevated during the experiment under 200MPa_110°C, we evaluated frictional coefficients with and without pore fluid pressure. We calculated effective pressures under 200MPa_110°C by assigning the recurrence intervals in Equation (1) and derived pore fluid pressure by subtracting effective pressure from the experimental confining pressure of 200 MPa. If the pore fluid pressure is not taken into account, the strength of the sample declining gradually with time shows anomalously high frictional coefficient ($> 1$) with a negative cohesion (Figure 5a). However, assuming the existence of pore fluid pressure, frictional coefficients were estimated to be approximately 0.6 (Figure 5 and Table S2), which is consistent with that of previous study (Scuderi et al., 2013). This also indicates that the temporal reduction in strengths of the sample under 200MPa_110°C is attributed not to the change of physical property but the generation of pore fluid pressure. Therefore, we conclude that the gradual change in slip behavior during the experiment under 200MPa_110°C originated from the elevated pore fluid pressure controlled by

269  dehydration kinetics of bassanite gouges. The crystalline system of anhydrite is hexagonal for
270  soluble anhydrite and orthorhombic for insoluble anhydrite (Freyer & Voigt, 2003). Under
271  200MPa_110-180°C, the crystalline system may have fully changed into insoluble anhydrite due
272  to the rapid dehydration reaction, leading to inhibition of rehydration after the experiment.
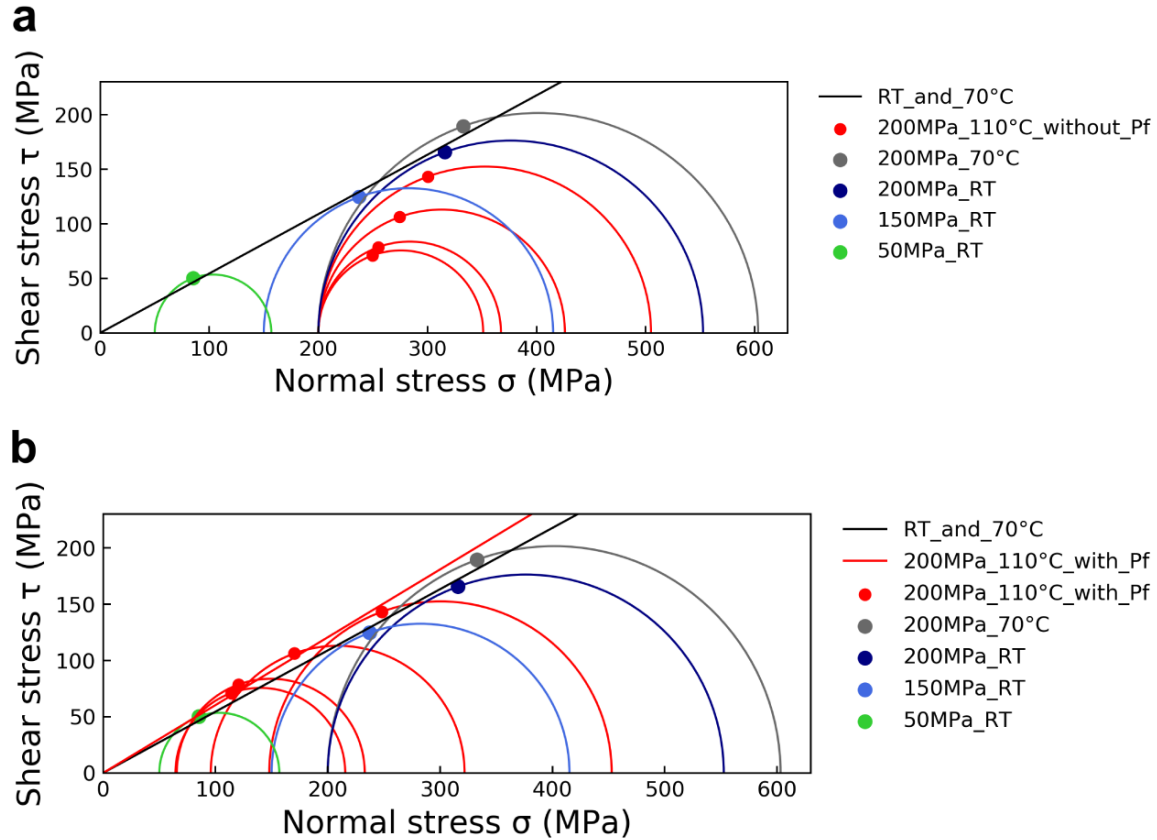
273



274

275         **Figure 5. Mohr circle and Mohr-Coulomb yield criterion.** We compared frictional
276  coefficient **a** without pore fluid pressure and **b** with pore fluid pressure. First, we plotted Mohr
277  circle and points of normal stress and shear stress, using the data of experimental pressure,
278  differential stress and an axial angle of 35 degrees (see Table S2). Second, we fitted the points of
279  normal stress and shear stress to obtain yield criterion (assuming intercept is 0). The data for RT
280  and 70 °C conditions have a well-fitted yield criterion and the frictional coefficient is 0.54.
281  However, the trend for 200MPa_110°C without pore fluid pressure (red plots in **a**) differs from
282  that for RT and 70 °C conditions. Assuming pore fluid pressure calculated with equation (1) (red
283  plots in **b**), the data for 200MPa_110°C showed a similar trend to the data for RT and 70 °C
284  conditions, and frictional coefficient for 200MPa_110°C became 0.60. The analysis implies that
285  pore fluid pressure occurred during the experiment under 200MPa_110°C

286

287

288

289

290        4.2 Time evolution of pore fluid pressure based on Avrami kinetics

291        We calculated effective pressure at each stress drop event by assigning each recurrence
292    interval in equation (1), and plotted pore fluid pressures estimated by the difference between the
293    confining pressure and the effective pressure. In the plotting, we assumed pore fluid pressure was
294    linearly proportional to the volume fraction of transformed material. We used Avrami kinetics
295    (Avrami, 1940) for fitting as follows:

296

$$P_f(t) = A\{1 - \exp(-kt^n)\}, \#(2)$$

297

298        where $P_f(t)$ is pore fluid pressure in MPa and $t$ is elapsed time in s ($R^2 = 0.951$). Figure 6
299    shows that Avrami equation represents the temporal evolution of pore fluid pressures much more
300    accurately. Notably, that we could not fit the pore pressure evolution by the first order reaction,
301    especially in the middle of the reaction.

302        We obtained two important parameters in Avrami equation: the reaction rate $k = 9.15\times10^{-13}$ $s^{-3.72}$ and the exponent $n = 3.72$. According to Arrhenius equation, reaction rate decreases
304    exponentially with the reciprocal of temperature (Logan, 1982; Laidler, 1984), and also,
305    decreases exponentially with pressure (Zhang, 2008). Ballirano and Melis (2009) examined
306    dehydration kinetics of bassanite in air, and their reaction rate was $8.8\times10^{-5}$ $s^{-1}$ at 398 K (the
307    same temperature with our dehydrated condition considering frictional heating (Sibson, 1975)).
308    Our reaction rate obtained under much higher confining pressure is smaller than the value of the
309    previous research, which is consistent with the dependence of reaction rate on pressure and
310    temperature.

311        Regarding Avrami exponent $n$, we first used the first-order reaction equation ($n = 1$ in
312    equation 2) as the fitting function. However, we found that Avrami equation ($n = 3.72$), rather
313    than the first-order reaction equation ($n = 1$), most accurately represented the time evolution of
314    pore fluid pressures. Therefore, there is a difference of 2.72 in the exponent $n$ between the first-
315    order reaction model and Avrami theory. From the process of deriving Avrami equation, the
316    exponent $n$ becomes the sum of fractal dimension on the surface of reaction products (water and
317    anhydrate) $D_s$ and 1 (i.e., $n = D_s + 1$) (Shimakawa, 2012). Based on this, our fractal dimension on
318    the surface of reaction products becomes 2.72. It is considered that due to the involvement of
319    spatial parameters such as particle shape, a power of time appears in Avrami equation.
320    Additionally, when the fractal dimension 2.72 in space is converted to fractal dimension in the
321    two-dimensional space (2D cross-section) of the Euclidean geometry, the fractal dimension on
322    the surface of reaction products is estimated to be 1.72. This fractal dimension 1.72 represents
323    how water forms a network within the gouge. In other words, since water exists in the pores
324    between the gouge, the fractal dimension 1.72 has information on the pore structure within the
325    gouge. The fractal dimension on the fracture system of Riedel shear planes is known to be about
326    1.6 at the maximum (Hirata, 1989), which is smaller than that of the pore structure, 1.72. This
327    indicates that Riedel shear planes develop in some parts of the pore network, and the difference
328    in fractal dimensions (capacity dimension) on fracture systems between Riedel shear planes and

329 pore network considered from water network has the information on pore structure originally
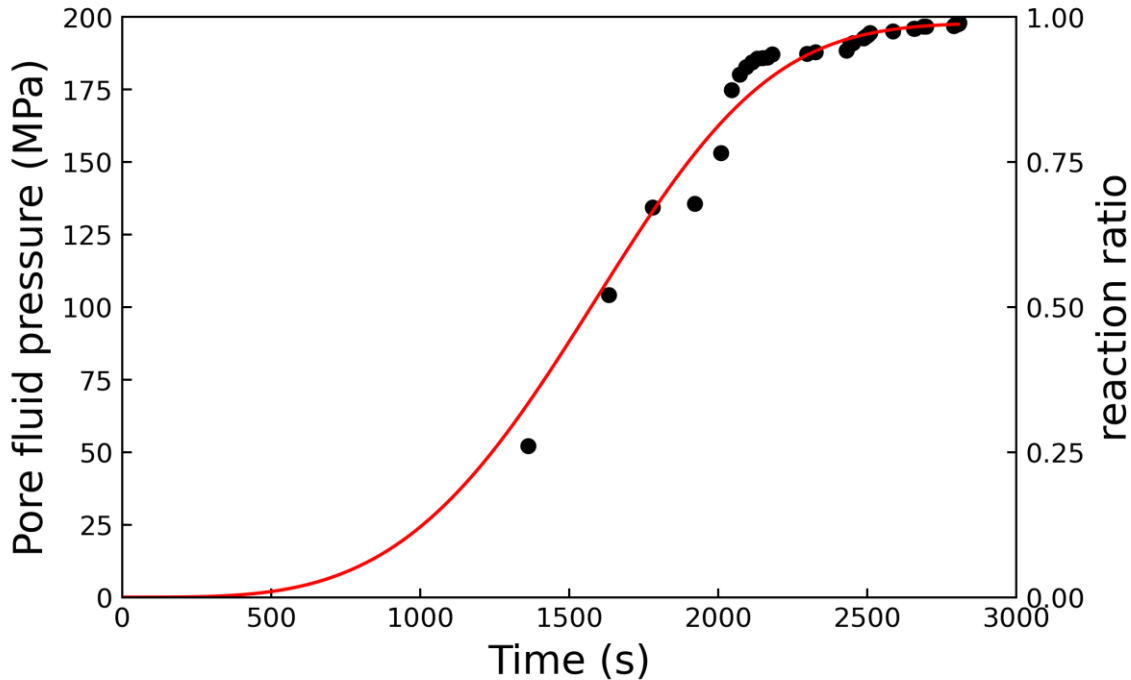330 present in the gouge.

331



332

333 **Figure 6. Estimated pore fluid pressure evolution (black dots) and prediction by**
334 **Avrami equation (red).**

335

336

337

338

339 4.3 Avrami kinetics and Weibull's fracture progression rates

340 In addition to the discussion on Avrami exponent, for the obtained function, the time
341 function of pore fluid pressure indicates the kinetically controlled degree of strength reductions,
342 in other words, the fracture progression rate. Moreover, if we view the separation reaction of a
343 substance, such as dehydration reaction, as a destructive process called decomposition, Avrami
344 equation can be regarded as Weibull cumulative distribution function which is often utilized for
345 describing the failure rate. Hence, it is assumed that Weibull cumulative distribution function has
346 a meaning not only of the failure rate but also the fracture progression rate. During our
347 deformation experiment conducted under 200MPa_110°C, four stick-slip events with large stress
348 drops occurred by 1921 s (corresponding to shear strain of about 3.5 in Figure 1b) after the start
349 of the experiment (see Figure S1). By substituting $t = 1921$ s in equation (2), the reaction ratio
350 was estimated to be approximately 80 %. This indicates that the high reaction progress rate close

351  to the completion of reaction controls the majority of the fracturing process, supporting that
352  Weibull cumulative distribution function also has a meaning of the fracture progression rate. In
353  other words, large stress drops were induced in the phase of the rapid increase in the reaction
354  ratio where the pore fluid pressure rapidly increased between 1360 and 1921 s in Figure 6
355  (corresponding to shear strain between 1.9 and 3.5 in Figure 1b). When the reaction progress rate
356  gradually decays where the rate of pore fluid pressure build-up decays after approximately 1921
357  s in Figure 6 (corresponding to shear strain of about 3.5 or greater in Figure 1b), slip events with
358  small stress drops dominated. This indicates that the reaction rate in Avrami equation also has a
359  meaning of the fracture progression rate via the Weibull function. The rate of increase in pore
360  fluid pressure affects the amount of stress drop, and therefore, we conclude that dehydration
361  kinetics of hydrous minerals control stick-slip behaviors.

362

## 363  5 Conclusions

364      We conducted deformation experiments using bassanite as an analogue material for
365  dehydrating system and reproduced dehydration instability in the laboratory. We demonstrated
366  the existence of dehydration-derived pore fluid pressure during our deformation experiment
367  under 200 MPa and 110 ℃ from the perspectives of microstructures and mechanical behaviors,
368  and derived the time function of pore fluid pressure based on Avrami kinetics. Moreover, the
369  Avrami equation provided the information on pore structures based on fractal geometry and
370  Weibull cumulative distribution function for the fracture progression rate. The analysis revealed
371  that the amount of slip was controlled by dehydration kinetics of hydrous minerals. The time
372  function of pore fluid pressure evolution derived from laboratory experiments contribute to better
373  understanding of the seismogenesis of deep and intermediate-depth earthquakes.

374

## 375  Data Availability Statements

376  The data in this study can be found in general repository.
377  (https://doi.org/10.6084/m9.figshare.25044524.v1)

378

383

384

## 385  References

386  Avrami, M. (1940), Kinetics of phase change. II Transformation-time relations for random
387      distribution of nuclei. The Journal of Chemical Physics, 8, 212–224.
388      https://doi.org/10.1063/1.1750631

389  Ballirano, P. & Melis, E. (2009), Thermal behaviour and kinetics of dehydration of gypsum in air
390      from in situ real-time laboratory parallel-beam X-ray powder diffraction. Phys. Chem.
391      Miner. 36, 391–402.

392  Brantut, N. *et al.* (2012), Dehydration-induced damage and deformation in gypsum and
393      implications for subduction zone processes. *Journal of Geophysical Research,* 117, 1–17.
394      https://doi.org/10.1029/2011JB008730

395  Chernak, L. J. & Hirth, G. (2011), Syndeformational antigorite dehydration produces stable fault
396      slip. *Geology,* 39, 847–850. https://doi.org/10.1130/G31919.1

397  Chollet, M., Daniel, I., Koga, K. T., Petitgirard, S. & Morard, G. (2009), Dehydration kinetics of
398      talc and 10 Å phase: Consequences for subduction zone seismicity. Earth and Planetary
399      Science Letters, 284, 57–64. https://doi.org/10.1016/j.epsl.2009.04.008

400  Freyer, D. & Voigt, W. (2003), Crystallization and Phase Stability of CaSO4 and CaSO4 –
401      Based Salts. Monatshefte für Chemie 134, 693–719. https://doi.org/10.1007/s00706-003-
402      0590-3

403  Gu, Y. & Wong, T. fong. (1994), Development of shear localization in simulated quartz gouge:
404      Effect of cumulative slip and gouge particle size. PAGEOPH 143, 387–423.
405      https://doi.org/10.1007/BF00874336

406  Hirata, M., Muto, J. & Nagahama, H. (2014), Experimental analysis on Rowe's stress-dilatancy
407      relation and frictional instability of fault gouges. *Episodes* 37, 303-307.
408      https://doi.org/10.18814/epiiugs/2014/v37i4/010

409  Hirata, T. (1989), Fractal dimension of fault systems in Japan: Fractal structure in rock fracture
410      geometry at various scales. *PAGEOPH* 131, 157–170.

411  Hirauchi, K. I. & Muto, J. (2015), Effect of stress state on slow rupture propagation in synthetic
412      fault gouges 4. Seismology. *Earth, Planets and Space,* 67, 25.
413      https://doi.org/10.1186/s40623-015-0199-x

414  Jayawickrama, E. G., Muto, J., Sasaki, O. & Nagahama, H. (2021), Damage Evolution of
415      Onnagawa Shale by Postmortem Thresholding of X-Ray Computed Tomography.
416      *Journal of Geophysical Research,* 126, 1–22. https://doi.org/10.1029/2021JB022056

417  Kirby, S. (1995), Interslab earthquakes and phase changes in subducting lithosphere. Reviews of
418      Geophysics, 33, 287–297. https://doi.org/10.1029/95RG00353

419  Laidler, K. J. (1984), The development of the arrhenius equation. Journal of Chemical Education
420      61, 494–498. https://doi.org/10.1021/ed061p494

421  Leclère, H., Faulkner, D., Wheeler, J. & Mariani, E. (2016), Permeability control on transient
422      slip weakening during gypsum dehydration: Implications for earthquakes in subduction
423      zones. *Earth and Planetary Science Letters,* 442, 1–12.
424      https://doi.org/10.1016/j.epsl.2016.02.015

Logan, S. R. (1982), The origin and status of the Arrhenius equation. J. Chem. Educ. 59, 279–281. https://doi.org/10.1021/ed059p279

Milsch, H. H. & Scholz, C. H. (2005), Dehydration-induced weakening and fault slip in gypsum: Implications for the faulting process at intermediate depth in subduction zones. Journal of Geophysical Research, 110, 1–16. https://doi.org/10.1029/2004JB003324

Mirwald, P. W. (2008), Experimental study of the dehydration reactions gypsum-bassanite and bassanite-anhydrite at high pressure: Indication of anomalous behavior of $H_2O$ at high pressure in the temperature range of 50-300 °C. *The Journal of Chemical Physics,* 128, 074502. https://doi.org/10.1063/1.2826321

Olgaard, D. L., Ko, S.-c. & Wong, T. (1995), Deformation and pore pressure in dehydrating gypsum under transiently drained conditions. Tectonophysics, 245, 237–248. https://doi.org/10.1016/0040-1951(94)00237-4

Onuma, K., Muto, J., Nagahama, H. & Otsuki, K. (2011), Electric potential changes associated with nucleation of stick-slip of simulated gouges. Tectonophysics 502, 308–314. https://doi.org/10.1016/j.tecto.2011.01.018

Perrillat, J. P. et al. (2005), Kinetics of antigorite dehydration: A real-time X-ray diffraction study. Earth and Planetary Science Letters, 236, 899–913. https://doi.org/10.1016/j.epsl.2005.06.006

Proctor, B. & Hirth, G. (2015), Role of pore fluid pressure on transient strength changes and fabric development during serpentine dehydration at mantle conditions: Implications for subduction-zone seismicity. Earth and Planetary Science Letters, 421, 1–12.

Raleigh, C. B. & Paterson, M. S. (1965), Experimental deformation of serpentinite and its tectonic implications. Journal of Geophysical Research, 70, 3965–3985. https://doi.org/10.1029/JZ070i016p03965

Scuderi, M. M., Niemeijer, A. R., Collettini, C. & Marone, C. (2013), Frictional properties and slip stability of active faults within carbonate–evaporite sequences: The role of dolomite and anhydrite. Earth and Planetary Science Letters, 369–370, 220–232. https://doi.org/10.1016/j.epsl.2013.03.024

Shimakawa, K. (2012), Dynamics of crystallization with fractal geometry: Extended KJMA approach in glasses. Phys. Status Solidi Basic Res. 249, 2024–2027. https://doi.org/10.1002/pssb.201200347

Shimazaki, K. and Nakata, T. (1980) Time-predictable recurrence model for large earthquakes. *Geophysical Research Letters* 7, 279-282. https://doi.org/10.1029/GL007i004p00279

Shiraishi, R., Muto, J., Tsunoda, A., Sawa, S. & Suzuki. (2022), A. Localized Deformation of Lawsonite During Cold Subduction. Journal of Geophysical Research, 127, e2021JB022134. https://doi.org/10.1029/2021JB022134

Sibson, R. H. (1975), Generation of pseudotachylyte by ancient seismic faulting. *Geophysical Journal of the Royal Astronomical Society* 43, 775–794. https://doi.org/10.1111/j.1365-246X.1975.tb06195.x

465 Tang, Y., Gao, J., Liu, C., Chen, X. & Zhao, Y. (2019), Dehydration Pathways of Gypsum and
466          the Rehydration Mechanism of Soluble Anhydrite γ-$CaSO_4$. *ACS Omega* 4, 7636–7642.
467          https://doi.org/10.1021/acsomega.8b03476

468 Yamasaki, T. & Seno, T. (2003), Double seismic zone and dehydration embrittlement of the
469          subducting slab. Journal of Geophysical Research, 108, 1–21.
470          https://doi.org/10.1029/2002JB001918

471 Zhang, Y. (2008), Geochemical Kinetics, Princeton University Press.
472

473